Non-topographic current contrast in scanning field emission microscopy

G. Bertolini[1], O. Gürlü[1,†], R. Pröbsting[1], D. Westholm[1], J. Wei[1], U. Ramsperger[1], D. A. Zanin[1], H. Cabrera[1], D. Pescia[1], J. P. Xanthakis[2], M. Schnedler[3] and R. E. Dunin-Borkowski[3]

[1] Laboratory for Solid State Physics, ETH Zurich, 8093 Zurich, Switzerland
[2] Electrical and Computer Engineering Department, National Technical University of Athens, Athens 15700, Greece
[3] Ernst Ruska-Centre for Microscopy and Spectroscopy with Electrons and Peter Grünberg Institute, Forschungszentrum Jülich, 52425 Jülich, Germany

In scanning field emission microscopy (SFEM), a tip (the source) is approached to few (or a few tens of) nanometres distance from a surface (the collector) and biased to field-emit electrons. In a previous study (Zanin et al. 2016 Proc. R. Soc. A 472, 20160475. (doi:10.1098/rspa.2016.0475)), the field-emitted current was found to change by approximately 1% at a monatomic surface step (approx. 200 pm thick). Here we prepare surface domains of adjacent different materials that, in some instances, have a topographic contrast smaller than 15 pm. Nevertheless, we observe a contrast in the field-emitted current as high as 10%. This non-topographic collector material dependence is a yet unexplored degree of freedom calling for a new understanding of the quantum mechanical tunnelling barrier at the source site that takes into account the properties of the material at the collector site.

1. Introduction

By the physical process of field emission, electrons, confined within a metal, tunnel quantum mechanically through a classically forbidden potential barrier, surrounding the emission site, to escape into vacuum [1–3]. The barrier width is decreased by the application of a suitably strong electric field, so that the phenomenon is also referred to as electric field-assisted quantum tunnelling. The electron beam produced in this way is used e.g. in the column of the most advanced electron microscopes [4]. If a 'collector' is placed a few nm to a few tens of nm distance from the emission site, a nanoscale junction is established that functions as the building block of a nanoscale vacuum channel transistor [5,6]. The proximity between tip and collector restricts the lateral size of the field-emitted beam: a lensless, 'nanoscale' electron microscope originates [7–9]. By recording the field emission current and the current of electrons escaping the tip–vacuum–collector junction, one atomic layer thick asperities at the collector site were imaged with 1 nm lateral spatial resolution [9]. Scanning tunnelling microscopy (STM) [10] (where the tip is held at subnanometre distances from the surface) achieves a better lateral spatial resolution but lacks the electronic system of the escaping electrons that appear in scanning *field emission* microscopy (SFEM) [7–9].

The quantitative understanding of field emission goes back to the dawn of quantum mechanics [1]. It foresees that the field-emitted current density is proportional to e^{-G}, the Gamov factor G behaving approximately as F^{-1}, with F being the electric field at the apex of the tip [1,2]. F is proportional to the magnitude of the electrostatic potential difference between the source and the collector. The proportionality constant [1,2,11] β depends primarily on the geometry of the source: for instance, it can be enhanced by sharpening the tip to nanometre scale radius of curvature [11]. Vertical asperities at the collector site change the effective distance Z between tip and collector, thus affecting β ([12,13] and references therein). The *Z*-dependence of β has been verified experimentally [9]: a monatomic surface step (approx. 200 pm), imaged in SFEM at an average distance of 6–10 nm, changes the field emitted current by approximately 1%.

In this work, we have prepared surfaces with different materials residing next to each other on nanometre lateral scale, with the aim of determining the limits of vertical resolution in SFEM. The dual system primarily studied here consists of p(1 × 1) tungsten domains (referred to for simplicity as 'W') versus R(15 × 12) tungsten carbide-domains ('WC'), appearing on a W(110) surface upon a suitable sample handling protocol. The vertical corrugation introduced by C-reconstructed domains is less than 15 pm. Surprisingly, when we move the tip from a W domain to a WC domain, we observe changes of the field-emitted current of approximately 10%, i.e. two orders of magnitude larger than expected on the base of *Z*-changes. Preliminary results have been published in a conference proceedings [14].

2. Experimental results

During the STM and SFEM experiments, the base pressure was less than 2.0×10^{-11} mbar and the sample was at room temperature. The surface topography is detected, in this work, by STM

imaging. STM is performed in the constant current mode, i.e. the tip is displaced vertically by a feedback loop in order to keep the tunnelling current constant ('red' in the schematic illustration figure 1a of the 'constant current' STM mode). The applied voltage U is typically less than 1 V and the tunnelling currents are approximately 300 pA. The subsequent field emission imaging is primarily performed in a 'constant height' mode (figure 1b): the software interpolates the tip displacements, encoded during previous STM imaging, as a function of the lateral coordinate, by means of a mathematical plane. This defines a planar coordinate system parallel to the previously imaged area along which the tip is translated during field emission imaging. The quantity recorded in this mode is no longer the vertical tip translation but the current absorbed by the collector (I_c, red in figure 1b) or the current field-emitted by the source (I_s, blue in figure 1b).

The dual system on which we have focused the experimental work consists of domains of a two dimensional tungsten-carbide reconstruction (technically: W(110)/C − R(15 × 12) [15,16], referred to here as 'WC' for simplicity) embedded within large regions of the 'clean', p(1 × 1) phase ('W') of a W(110) single crystal surface. The preparation of the dual W-WC sample starts with the cleaning of the W(110) single crystal [15]. The bulk of a W crystal always contains a few per cent of C left behind during crystal growth. When the sample is flashed to approximately 2300 K, C segregates to the surface and builds locally two surface carbides known as W/C − R(15 × 3) and W/C − R(15 × 12) [15,16] reconstructions. After repeated flashing we find predominantly the W/C − R(15 × 12) reconstruction. If the cooling down is fast enough, the W/C − R(15 × 12) reconstruction, which is referred to as metastable in [15], is preserved and is found locally next to regions of 'clean', p(1 × 1) − W(110); see, for example, the STM image figure 2a. The formation of the W/C − R(15 × 12) nanomesh is revealed in the STM image figure 2b (not atomically resolved) by the typical pattern of periodically ordered larger and smaller bright spots, arranged along 'rows' repeating approximately every 3 nm. We observe that the average vertical corrugation in the carbidic phase is approximately 10 pm. The relative displacement of the two phases is approximately 5 pm (figure 2c). The SFEM experiment starts with the harvesting of the WC domains by conventional STM. Figure 3a shows a set of W terraces separated by monatomic steps, running along the diagonal of the image. As STM imaging is performed in constant current mode, the colour code describes the relative height of the terraces with respect to the lowest one on the right-hand side. There are some point defects spread across the image, but also domains with a faint, streak-like corrugation, hosting the carbidic reconstruction (see e.g. the middle terrace). The reconstruction appears 'faint', i.e. in the vertical scale used to render the monatomic steps (which are approx. 200 pm thick, i.e. approx. 10 times thicker than the WC corrugation). Figure 3b was taken over the same surface region depicted in figure 3a but in the field emission regime (Z = 20 nm, U = 41 V). The image displays I_c, coded as specified by the vertical bar. The regions corresponding to the WC domains appear brighter, indicating an enhancement of I_c. For this image, the average I_c contrast, defined as $(I_c^{WC} - I_c^{W})/(I_c^{WC} + I_c^{W})$ between WC and W (the extraction of the contrast from images is explained in appendix A) is approximately 17%. The image is taken by scanning along horizontal lines, from the top to the bottom. During imaging (the time for scanning one horizontal line, consisting of 256 pixels, is typically 2 s) instabilities of the field-emitted current introduce noise into the image. To partially eliminate this noise, I_c of figure 3b is divided by the average value along the horizontal line and plotted (colour code in the vertical bar) in figure 3c (superposed onto the STM image). As the images show, the change of I_c is as local as the boundary between WC and W (approx. 5 nm, see appendix A).

For technical reasons, in figure 3 we did not measure Is but I_c. Therefore, a situation is possible where I_s is the same over WC and W, and the contrast in I_c is compensated by a contrast carried by those electrons that escape the junction [9]. Two experimental facts prove that this situation does not occur. First, we have imaged the same domains simultaneously to I_c using those electrons that escape the junction ('green' in figure 1b, see also appendix B). We observe an enhanced count rate on top of WC in this channel of detection as well, producing a contrast with the same sign as I_c. Second, we have implemented the simultaneous recording of I_c and I_s in a different experiment and taken images of the same surface region at different values of U in both channels of detection: I_c and I_s. The two currents are necessarily measured with two different current amplifiers which are only nominally identical but, in practice, can have some instrumental multiplicative offset. We estimate this offset to be approximately 1%. The resulting $I_c(U)$ and $I_s(U)$ are displayed in figure 4a. The values of the

current were obtained by averaging over the respective domains. Within the margin of instrumental uncertainty, the currents in the two channels coincide and both are enhanced on WC. We can therefore state with certainty that the region of the collector residing just in front of the tip apex participates in the formation of the tunnelling barrier at the source site. The dependence on the collector of the field-emitted current with a similar order of magnitude is recorded systematically for further dual systems, see appendix D. As an example, we plot in figure 4b $I_s(U)$ and $I_c(U)$ curves recorded on a dual system consisting of W (red circle in the inset) versus Fe-covered WC (blue square). The sample preparation is explained in appendix D. In figure 4b, the current–voltage characteristics are taken by keeping the tip at a fixed position on top of the two different surface domains. The elimination of current fluctuations and noise is particularly important when comparing simultaneously measured $I_s(U)$ and $I_c(U)$ curves. Since the current is measured on the same wire that brings the bias to the tip or the sample, when one of the two electrodes is subject to a change of the bias in time the current measured on it is also affected by such change, showing possibly a capacitative response. Accordingly, the system needs a certain amount of time to relax after setting a certain voltage. In our system, this relaxation time is required on the I_s channel when the tip voltage is varied. We estimated that a relaxation time of 100 ms between consecutive current measurements is needed after U is changed. Using shorter times resulted in current– voltage characteristics measured forwards (i.e. by increasing U) and backwards (i.e. by decreasing U) not to coincide. The acquisition time was set, accordingly, to 100–200 ms. We learn from figure 4a,b that (i) I_s and I_c almost coincide, leaving the number of electrons escaping the junction in the 1% range, and (ii) the field-emitted current contrast is significantly larger than expected from the vertical corrugation.

3. Discussion

A 10% current contrast can be achieved if one assumes that some characteristics of the tip, such as its work function ϕ_{tip} (we recall that $G \propto (\phi_{tip})^{3/2}$ [1]) or its effective emission area (entering the current as a prefactor to the exponential) change when the tip is moved from one domain to the other. In fact, one can obtain a good fit of the experimental $I(U)$ curves of figure 4 by adapting the tip work function. However, during imaging, such a change must occur reversibly and exactly in correspondence with the domain boundary. For example, a picking up of some atom by the tip when on top of WC should be followed by a release of it when the tip is on W and a picking up of the same atom in the same position again when re-entering the WC domain. A reversible change of the tip parameters therefore seems very improbable, also because one should find it for any of the dual systems reported in appendix D.

The only parameters remaining for explaining the contrast are β and U, entering the electric field F at the emission site, $F = \beta \cdot U$. It is known that $\beta = \beta(Z)$ [9,12,13], i.e. a vertical corrugation on the collector site is bound to change Z and with it the electric field at the apex [2,12,13]. In the present work, we have taken care of harvesting specifically those WC domains that are embedded within the same terrace as the neighbouring W domains (figure 2a), so that the only vertical corrugation left when going from WC to W is that entailed by the WC corrugation or by a displacement on the entire WC domains with respect to the W domains. This corrugation is, however, only a few pm (figure 2c) and can only produce a contrast of the field-emitted current that is approximately two orders of magnitude smaller [9] than that observed here.

As originally predicted by Simmons [17], the work function difference $\varphi_{tip} - \varphi_{collector}$ between tip and collector changes the magnitude of the electrostatic potential difference between the tip and collector from the applied voltage U (the difference between the Fermi levels of tip and collector) to ($U + ((\phi_{tip} - \phi_{collector})/e)$) ($e$: magnitude of the electron charge). It is therefore necessary to ascertain any work function changes between W and WC domains. In appendix C, we have determined work function changes using the Gundlach regime of STM [18–21]. We find that $(\phi_{WC} - \phi_W)/e \approx -0.1$ V. To explore in a quantitative way the role of $\phi_{collector}$ on the current, we simulate current–voltage characteristics for a model system consisting of a metallic tip (modelled as a hyperboloid of revolution) with work function 4.5 eV at a variable distance Z from a planar collector. For the simulation of the current–voltage characteristics in the field emission regime, we employed a software package [22,23] that first solves the Poisson equation as well as the drift and diffusion equations for a tip–vacuum–sample system in three dimensions by a finite-difference scheme. The sample surface is assumed to be planar, while the metal tip is modelled as a hyperboloid of revolution. Image potential terms are included. The resulting electrostatic potential

along the central axis through the tip apex is used, in a second step, to derive a current through the vacuum barrier by employing the model of Bono and Good [24,25]. In their model, the transmission probability is approximated by ordinary Wentzel–Kramer–Brillouin (WKB) formulae. For electrons with a kinetic energy (in normal direction) above the vacuum barrier, the transmission probability is one. Accordingly, this model can be seen as a first approximation of the field emission current in the Fowler–Nordheim regime. A tip radius of 4 nm and opening angle of 7° were chosen, to better suit the experimental situation [13]. The work function of the tip was set to 4.5 eV. The work function of the sample was set to either 4.0 or 3.5 eV. The software package was developed primarily for semiconducting samples. In order to approximate a metal sample, we assumed a negligibly small band gap of 0.1 eV (negligible with respect to the work function change assumed in the simulations), a density of states effective mass of 1 and a carrier concentration of the order of 10^{20} cm^{-3}. Furthermore, in order to rule out a penetration of the electric field into the sample completely, the relative permittivity was set to a value close to zero. The inset of figure 5 shows simulated $I(U)$ for Z = 13 nm and for $\phi_{collector}$ = 4.0 eV (squares) and $\phi_{collector}$ = 3.5 eV (circles). The 'square' data points can be fitted by a Fowler–Nordheim functional dependence $I = a \cdot U^2 \cdot e^{-(b/U)}$ (a, b being some suitable parameters). The circular data points can be fitted with the same functional law, with the same fitting parameters a, b but with U replaced by $U - 0.4987$ V. The potential shift of −0.4987 V reproduces the collector work function difference of −0.5 eV assumed for the simulations. The simulated data have a general comprehensive symmetry: all simulated data points, computed for Z = 4, 9, 11, 13, 20 nm and for $\phi_{collector}$ = 3.5 eV and $\varphi_{collector}$ = 4 eV collapse, almost perfectly, onto one single graph when the current is plotted as a function of the shifted and rescaled voltage $\tilde{U} \doteq R(Z) \cdot (U + c)$ (figure 5). The multiplicative factor $R(Z)$ corrects for the different values that the parameter b acquires at different distances [13]. The shift parameter c is 0 for $\phi_{collector}$ = 4.0 eV and $c \approx -0.5$ V for $\phi_{collector}$ = 3.5 eV, independent of (Z, U). The systematic rigid shift used to explain the simulated data points is in line with Simmons' analytic results [17]. Notice that for the simulations we have assumed a work function difference of 0.5 eV for the convenience of display: in fact, in the simulations, the experimental work function difference of 0.1 eV would produce barely distinguishable $I(U)$ curves! We conclude that the experimentally observed current contrast is too large to be explained by a difference of the work function on the collector site, although, taking into account all data, also those shown in appendix D, it seems that the sign of the current contrast is determined by the sign of the difference between the work function, namely, the source current increases with a decrease in the work function of the collector. We are therefore left with a result which we do not completely understand, at least from the quantitative point of view.

There is, however, a degree of freedom that we have not considered yet. We know that the electric field at the source site is approximately 6 V nm^{-1} during field emission [13]. By virtue of the boundary conditions, an electric field at the tip translates to the region of the collector residing in front of the tip. The electric field at the collector site, which is only a few nanometres away from the tip, is still sizeable (approx. 2 V nm^{-1} [26]). An electric field at the surface of a metal, pointing from the metal to the vacuum, is known to increase the work function approximately linearly with its strength. The change is material dependent [27–32] and can be of the order of 0.4–0.8 eV @ 2 V nm^{-1} (see e.g. fig. 3 in [27]). This new degree of freedom introduces the possibility that the applied potential U is not rigidly shifted as in the model of Simmons [17] but is shifted by a term that is linear in U, i.e. that the parameter c, assumed to be a constant in this work, is actually proportional to U. This mechanism introduces an effective dependence of β (i.e. the fitting parameter b) from the material residing at the collector site. If one uses this new degree of freedom to fit the measured $I(U)$ characteristics, one finds that a relative change $(\beta_{WC} - \beta_W)/\beta_W$ of the order of approximately 3–8% explains the observed current–voltage characteristics better than a rigid shift. However, we do not have any sign of a material-dependent work function change in the low and intermediate voltages modes of STM. A more quantitative discussion that treats on an equal footing the various regimes of STM (the tunnelling, the Gundlach and the field emission regime) is therefore, at this point, mandatory.

Funding

The research was partially funded by Marie Curie Initial Training Network (ITN), grant no. 606988 under FP7-PEOPLE-2013-ITN, the Swiss National Science Foundation (SNF grant no. 20-134422) and

the Commission for Technology and Innovation (CTI grant no. 9860.1 PFNM-NM).

Acknowledgements

O.G. thanks M. Erbudak and E. Tosatti. D.P. thanks A. Kyritsakis and C. Walker for helpful discussions. D.P., G.B., J.W., D.W. and U.R. thank R. Forbes for helpful discussions.

References

1. Murphy E.L., Good R.H., *Phys. Rev.* **102**, 1464–1473, 1956 (doi:10.1103/PhysRev.102.1464)

2. Forbes R.G., *Ultramicroscopy* **79**, 11–23, 1999 (doi:10.1016/S0304-3991(99)00097-2)

3. Lepetit B., J. Appl. Phys. **122**, 215105, 2017 (doi:10.1063/1.5009064)

4. Williams D.B., Carter C.B. Electron sources, *In* "Transmission electron microscopy" (eds. D.B. Williams, C.B. Carter), pp. 73–89 Boston, MA: Springer, 2009 (doi:10.1007/978-0-387-76501-3)

5. Han Jin-Woo, Moon Dong-Il, Meyyappan M., *Nano Lett*. **17**, 2146–2151, 2017 (doi:10.1021/acs.nanolett.6b04363)

6. Tsagarakis M.S., Xanthakis J.P., *AIP Adv.* **9**, 105314, 2019 (doi:10.1063/1. 5123280)

7. Young R, Ward J, Scire F., *Rev. Sci. Instrum.* **43**, 999–1011, 1972 (doi:10.1063/1.1685846)

8. Festy F., Palmer R.E., *Appl. Phys. Lett.* **85**, 5034—5036, 2004 (doi:10.1063/1.1818742)

9. Zanin D.A., De Pietro L.G., Peter Q., Kostanyan A., Cabrera H., Vindigni A., Bähler Th., Pescia D., Ramsperger U., *Proc. R. Soc. A* **472**, 20160475, 2016 (doi:10.1098/rspa.2016.0475)

10. Stroscio J.A., Feenstra R.M., "Tunneling spectroscopy" *In* Scanning tunneling microscopy, vol. 27 (eds. J.A. Stroscio, W.J. Kaiser), pp. 96–145, Boston, MA: Academic Press, 1993

11. Kyritsakis A., Xanthakis J.P., *Proc. R. Soc.* A **471**, 20140811, 2015 (doi:10.1098/rspa.2014.0811)

12. Zuber J.D., Jensen K.L., Sullivan T.E., *J. Appl. Phys.* **91**, 9379, 2002 (doi:10.1063/1.1474596)

13. Cabrera H. *et al.*, *Phys. Rev. B* **87**, 115436, 2013 (doi:10.1103/PhysRevB.87.115436)

14. Westholm D., Wei J., Bertolini G., Gürlü O., Pescia D., Ramsperger U., "Non-topographic contrast in constant-current scanning fieldemission microscopy (SFEM)" *In* 33rd Int. Vacuum Nanoelectronics Conference (IVNC), Lyon, France, 6–10 July, pp. 1–2., Piscataway, NJ: IEEE., 2020 (doi:10.1109/IVNC49440.2020.9203360)

15. Varykhalov A., Rader O., Gudat W., *Phys. Rev. B* **77**, 035412, 2008 (doi:10.1103/PhysRevB.77.035412)

16. Bode M., Pascal R., Wiesendanger R., *Surf. Sci.* **344**, 185–191, 1995 (doi:10.1016/0039-6028(95)00873-X)

17. Simmons J.G., *J. Appl. Phys*. **34**, 2581, 1963 (doi:10.1063/1.1729774)

18. Jason A.J., Burns R.P., Inghram M.G., *J. Chem. Phys*. **43**, 3762–3763, 1965 (doi:10.1063/1.1696550)

19. Lin C.L., Lu S.M., Su W.B., Shih H.T., Wu B.F., Yao Y.D., Chang C.S., Tsong Tien T., *Phys. Rev. Lett*. **99**, 216103, 2007 (doi:10.1103/PhysRevLett.99.216103)

20. Becker M., Berndt R., *Phys. Rev. B* **81**, 035426, 2010, (doi:10.1103/PhysRevB.81.035426)

21. Jung T., Mo Y.W., Himpsel F.J., *Phys. Rev. Lett.* **74**, 1641–1644, 1995 (doi:10.1103/PhysRevLett.74.1641)

22. Schnedler M., Dunin-Borkowski R.E., Ebert Ph., *Phys. Rev. B* **93**, 195444, 2016 (doi:10.1103/PhysRevB.93.195444)

23. Schnedler M., Portz V., Weidlich P.H., Dunin-Borkowski R.E., Ebert Ph., *Phys. Rev. B* **91**, 235305, 2015 (doi:10.1103/PhysRevB.91.235305)

24. Bono J., Good R.H., *Surf. Sci.* **175**, 415–420, 1986 (doi:10.1016/0039-6028(86)90243-8)

25. Feenstra R.M., Stroscio J.A., *J. Vac. Sci. Technol. B* **5**, 923–929, 1987 (doi:10.1116/1.583691)

26. De Pietro L.G., "Field emission scanning tunnelling microscopy with spin polarisation analysis", figure 2.6., Dissertation ETHZ Number **23714**, 2016 (doi:10.3929/ethz-a010792873).

27. Zhu Z.Z., Hou Z.-F., Huang M.-C., Huang R.-B., Zheng L.-S., *Chin. Phys. Lett.* **18**, 1111–1113, 2001 (doi:10.1088/0256-307X/18/8/339)

28. Inglesfield J.E., *Phil. Trans. R. Soc. Lond. A* **334**, 527–538, 1991 (doi:10.1098/rsta.1991.0032)

29. Kyritsakis A., Baibuz E., Jansson V., Djurabekova F., *Phys. Rev. B* **99**, 205418, 2019 (doi:10.1103/PhysRevB.99.205418)

30. Jensen K.L., *J. Vacuum Sci. Technol. B: Microelectron. Nanometer Struct.* **17**, 515–519, 1999 (doi:10.1116/1.590664)

31. Theophilou A.K., Modinos A., *Phys. Rev. B* **6**, 801–812, 1972 (doi:10.1103/PhysRevB.6.801)

32. Wang Y., Xu L., Hsu H.-Y., Leung T.-C., Lin M.-C., *J. Vac. Sci. Technol. B* **38**, 022209, 2020 (doi:10.1116/1.5140750)

33. Bertolini G., "MatLab Library for field emission imaging contrast and resolution analysis", 2020 (doi:10.5281/zenodo. 3675443)

Figures

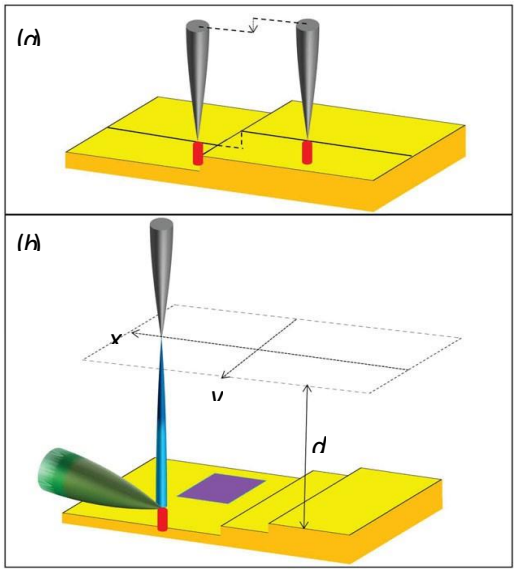

Figure 1. (a) Schematic view of the constant current STM imaging mode. The tip (grey) is displaced vertically (dashed arrow) when moved across a monatomic step on the surface (profiled by a dashed line) of the sample (yellow), so that the STM tunnelling current ('red' beam) is kept constant. (b) Schematic view of the constant height SFEM imaging. The tip is moved along a surface (dashed) which has a constant average distance d from the underlying surface (consisting of monatomic steps and including a 'purple' domain). The 'blue' beam represents the electrons field-emitted from the tip (I_s). The 'red' beam represents the electrons entering the sample (I_c). The 'green' beam shows those electrons that escape the tip–surface junction.

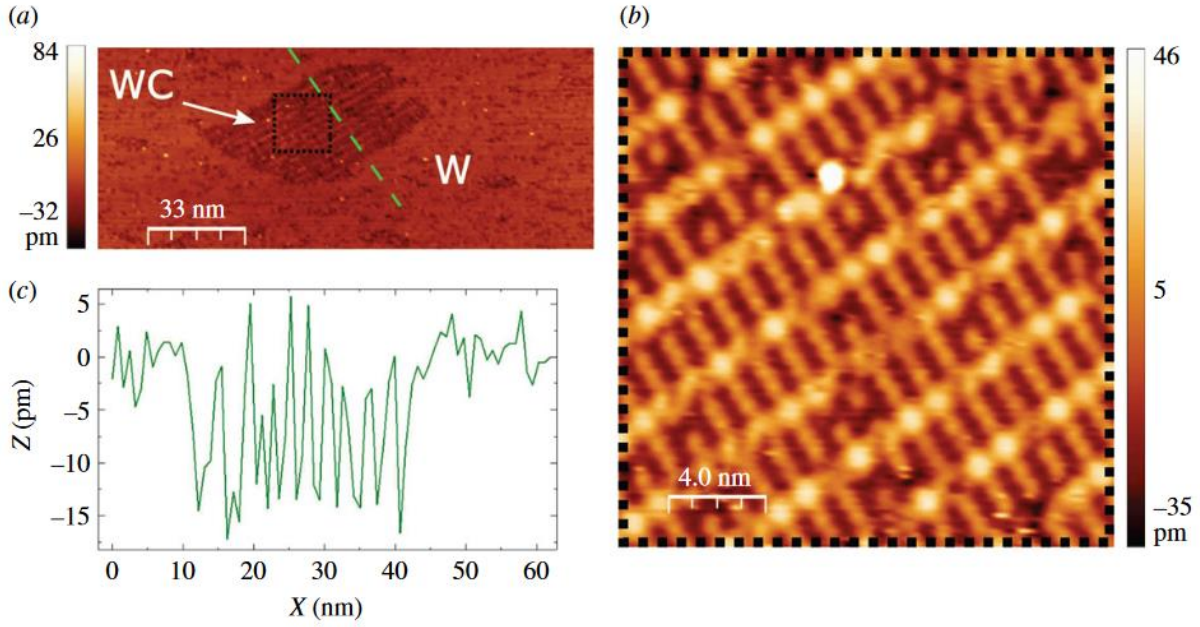

Figure 2. (a) STM topography of a W(110) surface. The tip vertical displacement is rendered with the colour code specified in the vertical bar. In the middle of the terrace, a domain of embedded carbide is visible. (b) 20 × 20 nm zoom of the black dotted frame in a showing the R(15 × 12) carbide reconstruction. (c) Height profile across the carbide domains (along the green path in a) revealing a maximum corrugation of less than 15 pm when moving from one region to the other. Scanning parameters: U = 0.9 V, current: 500 pA.

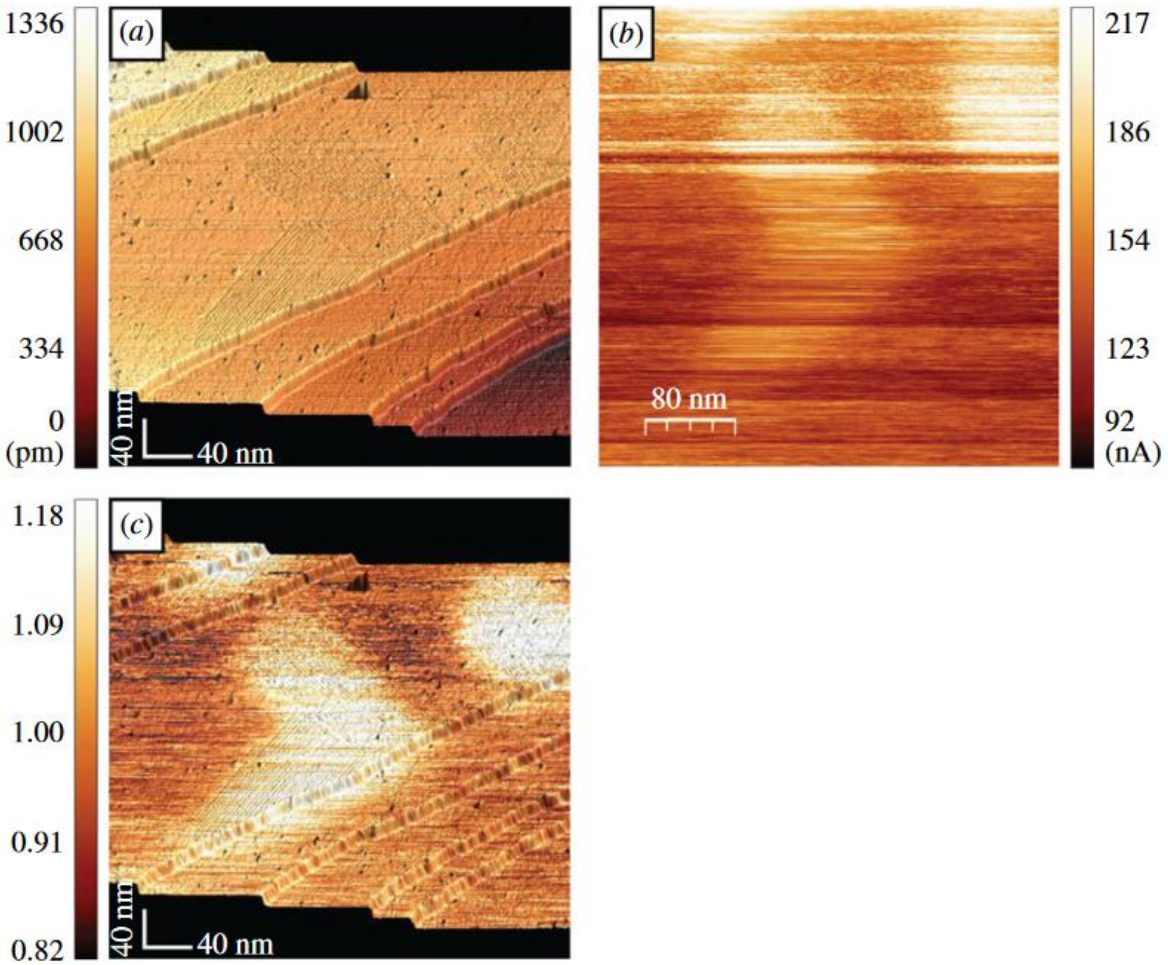

Figure 3. Field emission imaging. (a) STM image of the W(110) surface showing terraces separated by monatomic steps. The colour code in the vertical bar gives the position of the terraces with respect to the lowest one (darkest) on the right. The carbidic phase appears as a faint corrugation on some terraces. (b) The same region of the surface is imaged in the field emission regime (U = 41 V, Z = 13 nm). The colour code used to encode the absorbed current is given in the vertical bar. (c) The field emission image 3b (the current being divided by the line average) is superimposed onto the STM image 3a for clarity. The colour code used to encode the normalized current is given in the vertical bar.

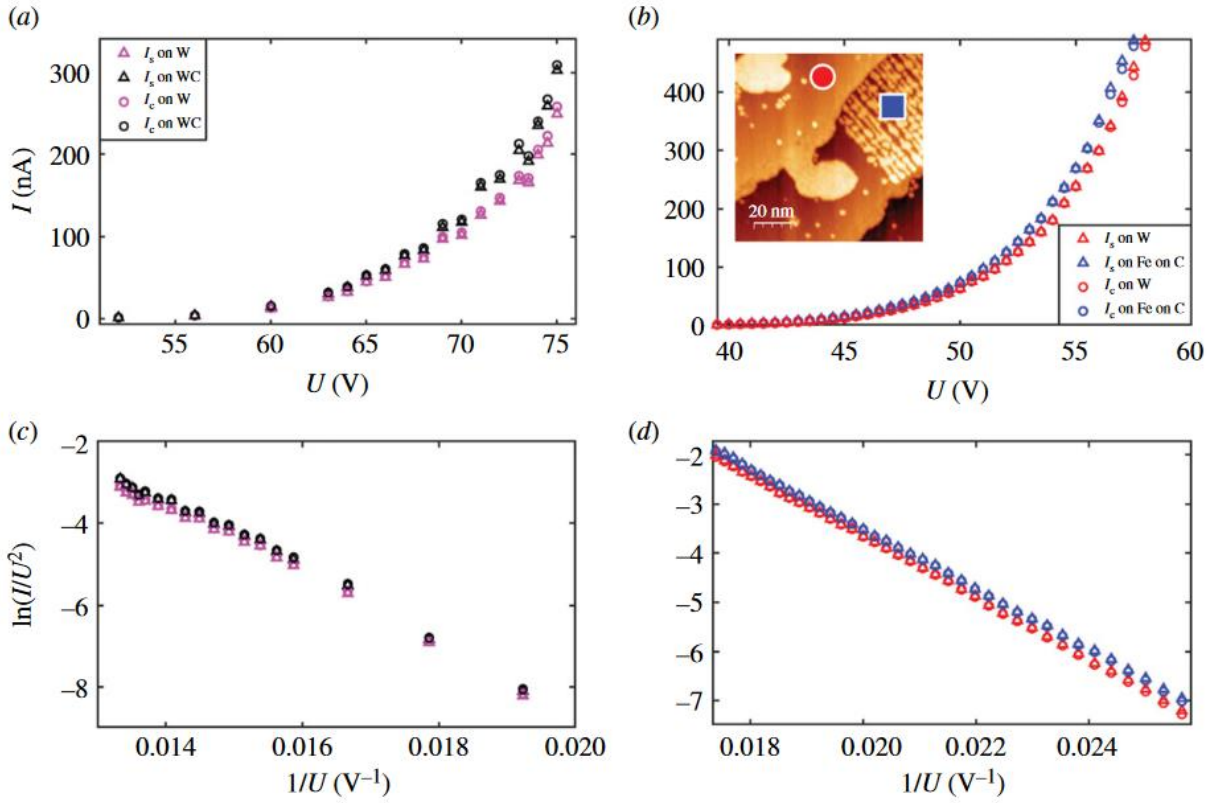

Figure 4. Current–voltage characteristics. (a) Obtained by spatial average of images of WC and W domains taken at Z = 26 nm. Black triangles: Is on WC. Black circles: I_c on WC. Pink triangles: I_s on W. Pink circles: I_c on W. (b) I_s and I_c as a function U for Fe on WC (blue triangles, respectively, blue circles) and W (red triangles, respectively, red circles), Z = 30 nm. Inset: STM image of the domains. The blue square (Fe on WC) and red circle (W) are the spots on top of which the current–voltage characteristics of figure 4b were measured. (c and d) The experimental data shown in a and b are plotted in a semilogarithmic scale (as Fowler–Nordheim plots) for more clarity in the low-voltage regime.

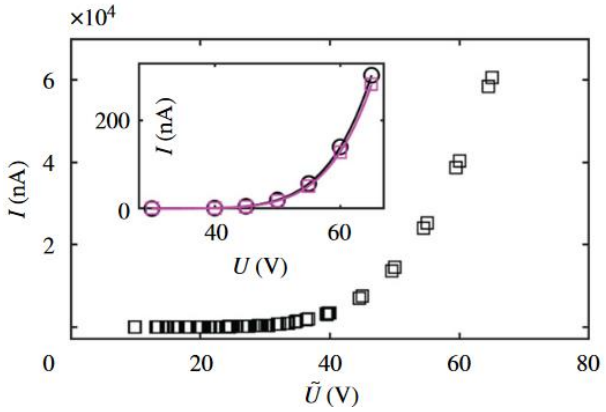

Figure 5. Simulated current–voltage characteristics. Inset: Z = 13 nm, circles: $\phi_{collector}$ = 3.5 eV, squares: $\phi_{collector}$ = 4.0 eV. Continuous lines are fits with a Fowler–Nordheim functional dependence $I = a \cdot U^2 \cdot \exp(-b/U)$ (squares) and $I = a \cdot U^2 \cdot \exp(-(b/(U + c)))$ (circles). Bulk: All simulated data points (Z = 4, 9, 11, 13, 20 nm and $\phi_{collector}$ = 3.5, 4.0 eV) plotted as a function of the rescaled variable $\tilde{U} \doteq R(Z) \cdot (U + c)$. c = 0 for $\phi_{collector}$ = 4.0 eV, c = −0.5 V for $\phi_{collector}$ = 3.5 eV.

Appendix

The appendix of this preprint can be found at https://doi.org/10.1098/rsos.210511